

Escaping Spectral Bias without Backpropagation:

Fast Implicit Neural Representations with Extreme Learning Machines

Woojin Cho ^{*1}

Junghwan Park ^{*1}

Abstract

Training implicit neural representations (INRs) to capture fine-scale details typically relies on iterative backpropagation and is often hindered by spectral bias when the target exhibits highly non-uniform frequency content. We propose ELM-INR, a backpropagation-free INR that decomposes the domain into overlapping subdomains and fits each local problem using an Extreme Learning Machine (ELM) in closed form, replacing iterative optimization with stable linear least-squares solutions. This design yields fast and numerically robust reconstruction by combining local predictors through a partition of unity. To understand where approximation becomes difficult under fixed local capacity, we analyze the method from a spectral Barron norm perspective, which reveals that global reconstruction error is dominated by regions with high spectral complexity. Building on this insight, we introduce BEAM, an adaptive mesh refinement strategy that balances spectral complexity across subdomains to improve reconstruction quality in capacity-constrained regimes.

1. Introduction

Implicit neural representations (INRs) provide a simple and flexible way to model data as continuous functions. Instead of storing discrete samples on a fixed grid, an INR learns a coordinate-based mapping that returns the signal value at any queried location (Essakine et al., 2024). This viewpoint naturally enables resolution-free evaluation, continuous resampling, and compact representations that transfer across discretizations. As a result, INRs have become a broadly useful parameterization for complex signals, ranging from images and shapes to spatiotemporal fields.

^{*}Equal contribution ¹TelePIX, Seoul, Republic of Korea. Correspondence to: Woojin Cho <woojin.py@gmail.com>, Junghwan Park <brian897743@gmail.com>.

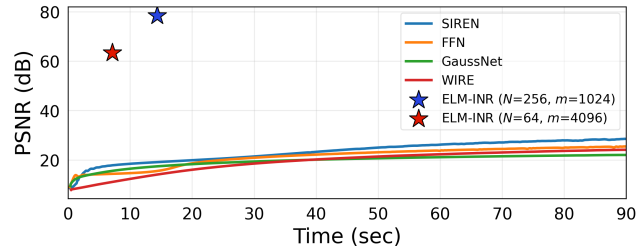


Figure 1. PSNR as a function of wall-clock time on the kodim05 image. Backpropagation-based INR baselines (SIREN, FFN, GaussNet and WIRE) are trained iteratively, while ELM-INR results correspond to closed-form solutions with different subdomain sizes and numbers of hidden nodes.

Despite these advantages, most INR pipelines still rely on iterative backpropagation to fit each instance. This makes optimization slow in wall-clock time, especially when the target contains fine-scale structures. The problem is amplified by spectral bias, where standard neural networks tend to learn low-frequency components early and fit high-frequency content much later, which can lead to delayed convergence or underfitting of localized details. In addition, compared to classical numerical analysis pipelines (Hildebrand, 1987; Reddy, 1993), the resulting learned models are often harder to interpret because the solution is embedded implicitly in network parameters produced by a nonconvex training process.

We propose ELM-INR to overcome both spectral bias induced slowdowns and lengthy iterative training. ELM-INR decomposes the domain into overlapping subdomains and fits each subproblem using an Extreme Learning Machine (ELM) whose output weights are obtained by a closed form least squares solve. The local predictors are then blended through a partition of unity to produce a smooth global reconstruction. This design removes end to end backpropagation and yields stable and predictable optimization behavior. Figure 1 illustrates this efficiency more concretely by reporting reconstruction quality over wall-clock time on the kodim05 image. While conventional INR baselines rely on backpropagation and therefore improve gradually through iterative optimization, ELM-INR is trained in a backpropagation-free manner and achieves high-quality reconstruction within a few seconds.

We further analyze ELM-INR through the lens of Barron space (Hildebrand, 1987; Marwah et al., 2023; Chen et al., 2021), using spectral complexity to explain why global reconstruction error is dominated by the most difficult regions. This perspective motivates BEAM, a Barron enhanced adaptive mesh refinement strategy that constructs spectrally balanced subproblems so that each local model uses its finite basis effectively. BEAM is especially beneficial in capacity constrained regimes where the number of basis functions is small, providing consistent gains without increasing iterative training cost.

Finally, we validate ELM-INR on diverse modalities beyond conventional images, including multispectral satellite imagery and scientific data such as Navier–Stokes, ERA5, and MRI. Despite using markedly less computation, our method consistently attains higher reconstruction quality, reaching approximately a $2\times$ PSNR gain over existing INR models in our benchmark settings.

To sum up, our contributions are threefold.

- We introduce a backpropagation-free INR framework based on closed form local ELM solves and partition of unity coupling.
- We provide a Barron space based explanation that links approximation difficulty to local spectral complexity and motivates spectral balancing.
- Finally, we propose BEAM, an adaptive partitioning algorithm that improves ELM-INR particularly when the local basis size is limited.

2. Related Work

Neural representations. Implicit neural representations (INRs), also known as coordinate-based neural fields, model a signal f as a continuous function $\hat{f} : \Omega \subset \mathbb{R}^d \rightarrow \mathbb{R}^c$ that maps coordinates to signal values (Sitzmann et al., 2020; Molaei et al., 2023; Cho et al., 2025b). Beyond 2D imagery, INRs are a standard parameterization in 3D vision where NeRF-style models represent scenes as continuous radiance and density fields and enable high-fidelity novel-view synthesis from multi-view observations (Mildenhall et al., 2021; Barron et al., 2021; Pumarola et al., 2021).

A chronic challenge is spectral bias because standard MLPs tend to fit low-frequency components earlier than high-frequency details, which can slow convergence and reduce fidelity on highly textured signals (Rahaman et al., 2019; Krishnapriyan et al., 2021; Yüce et al., 2022). To mitigate this issue, prior work enriches the input with frequency-rich encodings such as Fourier or positional features, or adopts periodic and localized function bases such as sinusoidal (Sitzmann et al., 2020), Gabor-like (Ramasinghe &

Lucey, 2022), or wavelet-like parameterizations (Saragadam et al., 2023).

Recently, another line of work leverages trained INRs as representations of individual instances in a dataset (Dupont et al., 2021; Cho et al., 2025a). In this view, each signal or field is first fit by an INR and the resulting parameters are then mapped to a vector space for retrieval, clustering, and conditional generation, while curated collections of pretrained INRs facilitate reuse and benchmarking across domains (Dupont et al., 2022; Ma et al., 2024; Jo et al., 2025). INRs have also been explored for compression by transmitting compact network parameters instead of raw pixels, yet most INR-based codecs still require per-instance iterative optimization at encoding time, which limits deployment under tight compute and power budgets (De Luigi et al., 2023; Bauer et al., 2023).

Backpropagation-free optimization and domain decomposition. Backpropagation-free learning is closely related to random feature models, where hidden layer parameters are frozen after initialization, reducing the training process to a linear regression problem solvable via efficient linear algebra routines rather than iterative gradient descent. A canonical instance is the Extreme Learning Machine (ELM) (Huang et al., 2006; 2011), which yields predictable runtimes and avoids local minima by solving for output weights in closed form. To handle multi-scale signals, Partition-of-Unity (PoU) methods (Babuška & Melenk, 1997; Lee et al., 2021) decompose the global domain into overlapping subdomains blended via smooth window functions, a concept foundational to methods like Generalized Finite Elements (Melenk & Babuška, 1996).

Recent works have extended these ideas to neural fields in scientific machine learning. For instance, FBPINNs (Moseley et al., 2021) and ELM-FBPINN (Anderson et al., 2024) demonstrate the potential of combining PINN (Raissi et al., 2019; Karniadakis et al., 2021) with domain decomposition to enhance stability. However, standard INRs continue to struggle with spectral bias and the computational cost of iterative backpropagation. Addressing these limitations, we propose ELM-INR, a method that integrates adaptive domain decomposition with the closed-form efficiency of ELMs to mitigate spectral bias and iterative optimization, enabling fast and high-fidelity reconstruction.

3. Extreme Learning Machines for Implicit Neural Representations

In this section, we develop the theoretical foundations of ELM-INR, our method that integrates Extreme Learning Machines with implicit neural representations. We first formalize how local function approximation is performed using ELMs, and how these local models are stitched together via

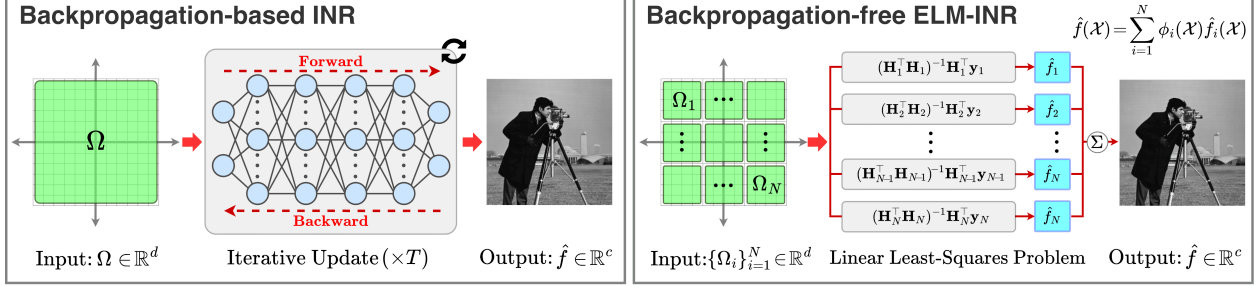


Figure 2. **Backpropagation-based INR vs. ELM-INR.** Standard INRs require iterative gradient-based training, while ELM-INR fits subdomain ELMs via one-shot least squares and blends them with partition-of-unity for a smooth global reconstruction.

a partition-of-unity to form a global approximation. We then analyze the computational complexity advantages of this approach. Finally, we introduce the Barron space framework to quantify the spectral complexity of target functions, which provides a rigorous motivation for our adaptive, spectral-based domain decomposition strategy leading into Section 4.

3.1. Local Approximation via ELMs

An ELM constitutes a single-layer feedforward network that avoids iterative optimization by fixing random hidden weights. Consequently, training reduces to solving a linear least squares problem in closed form. In our framework, we employ ELMs for local function approximation, which can be mathematically expressed as Eq. (1)

Definition 3.1 (Local Extreme Learning Machine). An ELM is a single-hidden-layer feedforward network where the input weights and biases are randomly initialized and frozen, while only the output weights are trainable. On a specific subdomain $\Omega_i \subset \mathbb{R}^d$, the local ELM $\hat{f}_i(\mathcal{X})$ is defined as follows:

$$\hat{f}_i(\mathcal{X}) = \sum_{j=1}^m \alpha_{i,j} \sigma(w_{i,j}^\top \mathcal{X} + b_{i,j}), \quad \forall \mathcal{X} \in \Omega_i \quad (1)$$

where m is the number of hidden neurons, $\sigma(\cdot)$ is the activation function, and $(w_{i,j}, b_{i,j})$ are fixed random parameters. The coefficients $\alpha_i = [\alpha_{i,1}, \dots, \alpha_{i,m}]^\top$ are the only trainable parameters for $\hat{f}_i(x)$.

Unlike conventional INRs that require iterative backpropagation, the fixed nature of the hidden parameters simplifies the learning process significantly. Since the mapping from the hidden layer to the output is linear, finding the optimal weights becomes a convex optimization problem.

Lemma 3.2 (ELM as Linear Least-Squares). *Training the local ELM \hat{f}_i on Ω_i reduces to a linear least-squares problem. Let $\mathbf{H}_i \in \mathbb{R}^{S_i \times m}$ be the hidden layer activation matrix for S_i sample points in Ω_i , defined as $(\mathbf{H}_i)_{kj} = \sigma(w_{i,j}^\top x_k + b_{i,j})$. The optimal output weights α_i^* that minimize the squared error $\|\mathbf{H}_i \alpha_i - \mathbf{y}_i\|_2^2$ can be obtained in closed form:*

minimize the squared error $\|\mathbf{H}_i \alpha_i - \mathbf{y}_i\|_2^2$ can be obtained in closed form:

$$\alpha_i^* = (\mathbf{H}_i^\top \mathbf{H}_i)^{-1} \mathbf{H}_i^\top \mathbf{y}_i \quad (2)$$

where $\mathbf{y}_i \in \mathbb{R}^{S_i}$ is the target vector sampled from the f at points inside Ω_i . This closed-form solution can be computed efficiently with standard linear solvers, enabling rapid training while avoiding sensitivity to local minima common in gradient-based optimization.

3.2. Global Reconstruction via Partition of Unity

To construct a continuous global representation $f(\mathcal{X})$ from these independent local models, we employ an overlapping domain decomposition strategy. We define a collection of smooth window functions $\{\phi_i(\mathcal{X})\}_{i=1}^N$ associated with the overlapping subdomains $\{\Omega_i\}_{i=1}^N$.

Definition 3.3 (Partition of Unity). The window functions are chosen to form a Partition of Unity (PoU) over the domain Ω :

$$\sum_{i=1}^N \phi_i(\mathcal{X}) = 1, \quad \forall \mathcal{X} \in \Omega, \quad \text{and} \quad \text{supp}(\phi_i) \subset \Omega_i. \quad (3)$$

The global ELM-INR approximation is then given by the weighted sum of local solutions:

$$\hat{f}(\mathcal{X}) = \sum_{i=1}^N \phi_i(\mathcal{X}) \hat{f}_i(\mathcal{X}). \quad (4)$$

This formulation ensures that the global approximation $\hat{f}(\mathcal{X})$ remains smooth and continuous across subdomain boundaries. Furthermore, because the global output is a linear combination of local outputs, the training remains decoupled; each α_i can be solved for independently, preserving the computational efficiency of the ELM framework.

3.3. Barron Space and Spectral Complexity

This section establishes the theoretical foundation for our proposed methods. It utilizes the Barron space framework

to quantify the spectral cost of approximating a function, proving that the global error of a neural representation is bottlenecked by regions with high spectral complexity.

Definition 3.4 (Barron Space \mathcal{B} and Function Class Γ (Bar-
ron, 2002)). The Barron space \mathcal{B} is a function space consisting of functions that can be efficiently approximated by shallow (single-hidden-layer) neural networks with dimension-independent error rates. Unlike classical Sobolev spaces (Adams & Fournier, 2003; Maz'ya, 2013), where approximation error suffers from the curse of dimensionality $\mathcal{O}(m^{-1/d})$, functions in the Barron space admit an approximation rate of $\mathcal{O}(1/\sqrt{m})$, where m is the network width (Ma et al., 2022).

To make this computationally tractable, the paper specifies a Fourier-based function class Γ as a concrete realization of the Barron space. This class is defined by the integrability of the function's Fourier spectrum and its first moment:

$$\Gamma := \left\{ f : \int_{\mathbb{R}^d} |\mathcal{F}(\xi)| d\xi < \infty, \int_{\mathbb{R}^d} \|\xi\|_1 |\mathcal{F}(\xi)| d\xi < \infty \right\}, \quad (5)$$

where \mathcal{F} denotes the Fourier transform of f and $\xi \in \mathbb{R}^d$ represents the continuous frequency variable.

Definition 3.5 (Spectral Barron Norm (Chen et al., 2021; Liao & Ming, 2025)). For a function $f \in \Gamma$, the difficulty of approximation is governed by the Spectral Barron Norm. This norm acts as a proxy for the function's spectral complexity, weighing the frequency components by their magnitude:

$$\|f\|_{\mathcal{B}_S} := \int_{\mathbb{R}^d} \|\xi\|_1 |\mathcal{F}(\xi)| d\xi. \quad (6)$$

Intuitively, a larger $\|f\|_{\mathcal{B}_S}$ indicates that the function possesses significant high-frequency energy or rapid variations, making it inherently harder for a neural network to fit.

This norm serves as a critical quantity in controlling the approximation error, as formalized by the following bound.

Theorem 3.6 (Approximation Error Bound). *For a function f with a finite spectral Barron norm $\|f\|_{\mathcal{B}_S}$, a neural network with m hidden units can approximate f on a compact domain Ω with an L^2 error bounded by:*

$$\|f - f_i\|_{L^2(\Omega)} \leq \frac{C\|f\|_{\mathcal{B}_S}}{\sqrt{m}}, \quad (7)$$

where C is a constant independent of m .

This theorem highlights a critical limitation of uniform partitioning. Real-world signals often exhibit non-uniform spectral complexity. If we employ a fixed width m across all subdomains, the global accuracy will be bottlenecked by the most complex region.

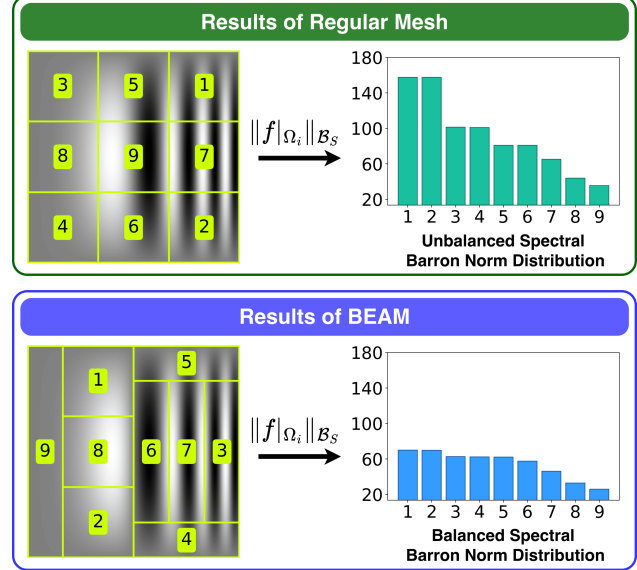


Figure 3. Comparison of Regular Mesh vs. BEAM. (Top) A regular uniform partition results in an unbalanced distribution of spectral Barron norms. (Bottom) BEAM adaptively partitions the domain. By merging simple regions and keeping complex regions small, it achieves a balanced spectral complexity distribution.

Remark 3.7 (Error Domination by Spectral Complexity). Consider a partition of Ω where each subdomain is approximated by an ELM of width m . Let $\beta_i := \|f|_{\Omega_i}\|_{\mathcal{B}_S}$ be the local spectral Barron norm. From Theorem 3.6, the worst-case local error is bounded by:

$$\max_i \|f - \hat{f}_i\|_{L^2(\Omega_i)} \leq \frac{C}{\sqrt{m}} \left(\max_i \beta_i \right). \quad (8)$$

Implication: The global reconstruction quality is limited by the region with the highest spectral complexity ($\max_i \beta_i$). This theoretical insight directly motivates our proposed method, Barron-Enhanced Adaptive Mesh refinement (BEAM), which adaptively partitions Ω to equalize β_i across all subdomains, ensuring uniform high-fidelity reconstruction.

4. Barron-Enhanced Adaptive Mesh

Building on the theoretical motivation established in Section 3, we propose BEAM (Barron-Enhanced Adaptive Mesh refinement). This domain decomposition algorithm is explicitly designed to equalize the spectral complexity across all subdomains. By strictly enforcing a spectral capacity constraint, BEAM transforms a computationally hard global fitting problem into a collection of spectrally balanced, manageable subproblems.

This design is directly motivated by the error bound in Eq. (8), which shows that the worst-case approximation error is governed by the largest local spectral Barron norm,

Algorithm 1 Barron-Enhanced Adaptive Mesh Refinement

Input: Image f , Threshold τ , Atomic size s
Output: Adaptive Partition \mathcal{P}

Initialize \mathcal{P} with $s \times s$ atomic cells; compute energies

repeat

- Sort $\Omega_i \in \mathcal{P}$ by energy (ascending)
- for** each Ω_i where $\|f|_{\Omega_i}\|_{\mathcal{B}_S} < \tau$ **do**

 - Find neighbor Ω_j that minimizes
 - $E_{new} = \|f|_{\Omega_i \cup \Omega_j}\|_{\mathcal{B}_S}$
 - if** $E_{new} \leq \tau$ **then**

 - Merge $\Omega_i, \Omega_j \rightarrow \Omega_{new}$ in \mathcal{P}
 - Update energy for Ω_{new} and remove Ω_i, Ω_j
 - end if**

 - end for**

until no merges occur

return \mathcal{P}

scaled by the inverse square root of the model capacity m . While increasing m can in principle suppress the error even in spectrally complex regions, doing so is often impractical in real-world INR settings due to computational, memory, or energy constraints. In such capacity-limited regimes, the dominant source of error arises from spectral imbalance across subdomains, and simply enlarging the model width becomes an inefficient remedy. BEAM addresses this issue by adaptively partitioning the domain to equalize local spectral Barron norms, thereby reducing the worst-case error under a fixed and moderate model capacity.

4.1. Practical Estimation of Spectral Barron Norm

Since the continuous spectral Barron norm is generally intractable to compute for real signals, we rely on a discrete Fourier-based spectral proxy (Marwah et al., 2023) that is suitable for finite data. For a region Ω_i , we compute spectral Barron norm as follows:

$$\|f|_{\Omega_i}\|_{\mathcal{B}_S} \approx \sum_k \|k\|_1 |\mathcal{F}_i(k)|, \quad (9)$$

where κ indexes discrete frequency components in the DFT domain. This measure directly reflects frequency-weighted spectral energy and is sufficient for BEAM, as the algorithm relies only on relative complexity comparisons under a threshold τ .

4.2. Principle of Spectral Balancing

Standard uniform partitioning fails to account for the spatial non-uniformity of signal complexity. To illustrate this, we consider a toy example derived from a Poisson equation with the target field $f(x_1, x_2) = \sin(2\pi(4x_1^3)) \sin(\pi x_2)$, which exhibits spatially varying frequencies due to the cubic term. Figure 3 demonstrates that applying a regular mesh to this field results in a highly skewed distribution of spectral com-

plexity: subdomains covering high-frequency oscillations exhibit excessive spectral Barron norms, creating error bottlenecks, while smooth regions remain underutilized.

BEAM addresses this imbalance by constructing a partition $\mathcal{P} = \{\Omega_i\}_{i=1}^N$ where every subdomain satisfies the spectral constraint $\|f|_{\Omega_i}\|_{\mathcal{B}_S} \leq \tau$. As visualized in the bottom panel of Figure 3, our algorithm adaptively merges simpler regions while isolating complex features, successfully equilibrating the spectral Barron norms across the domain. This ensures that the difficulty of each subproblem matches the capacity of the local ELM, preventing any single network from being overwhelmed.

4.3. Bottom-Up Spectral Merging

Unlike traditional top-down subdivision, BEAM employs a bottom-up merging strategy to allow flexible subdomain shapes, as summarized in Algorithm 1. The procedure initializes the domain as a fine grid of atomic cells and then iteratively identifies regions with low spectral complexity to merge them with spatial neighbors. To refine the partition, we use a greedy rule that evaluates all valid neighboring candidates and chooses the merge that minimizes the combined spectral energy while ensuring that it remains below the threshold τ . Repeating this step gradually aggregates background areas into larger subdomains while naturally isolating high-frequency details into smaller, dedicated patches.

Since the resulting subdomains can be irregular, we compute the spectral Barron norm on the bounding box of each region, masking pixels outside the region to zero to strictly evaluate the local signal content.

5. Experiments

Experimental Setup. We first describe the common experimental settings used throughout this section, including implementation details, baseline configurations, and the default setup of ELM-INR. All experiments are implemented in PyTorch (Paszke et al., 2019) and conducted on a workstation equipped with an NVIDIA A6000 GPU and an AMD EPYC 9224 24-Core processor. For baseline INR methods (SIREN (Sitzmann et al., 2020), FFN (Tancik et al., 2020), GaussNet (Ramasinghe & Lucey, 2022), and WIRE (Saragadam et al., 2023)), we use the Adam optimizer (Kingma, 2014) and tune model-specific hyperparameters; detailed configurations are provided in the Appendix C.

ELM-INR uses a single-hidden-layer Extreme Learning Machine with ReLU activations for all local models. Unless explicitly stated otherwise, we use square subdomains with $S_i = 32^2$ and fix the number of hidden nodes to $m = 1024$, shared across all subdomains; results reported without further specification correspond to ELM-INR without BEAM. Within each subdomain, pixel coordinates are normalized to

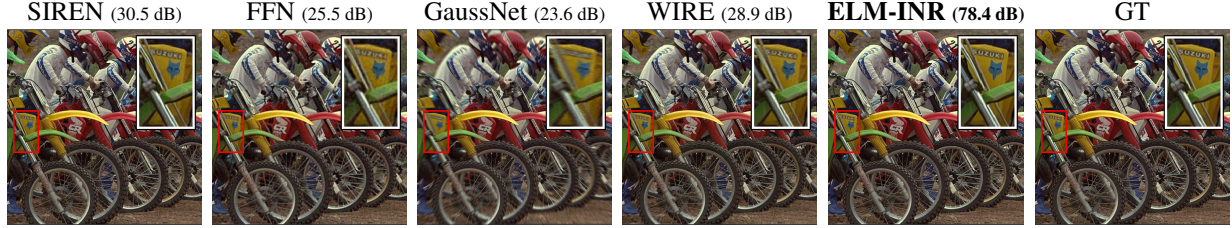


Figure 4. Qualitative comparison on the kodim05 image. All baseline models are trained for the same number of epochs.

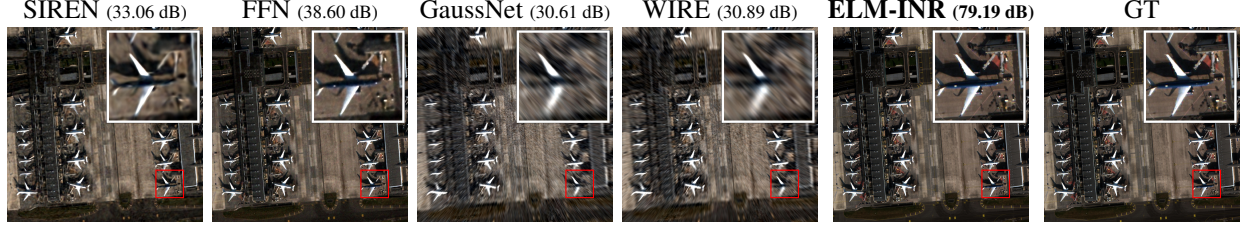


Figure 5. Qualitative comparison on a high-frequency region from a WorldView-3 multispectral image. The image consists of 8 spectral bands with a spatial resolution of 2048×2048 pixels, while the visualization shows only the RGB channels for clarity.

the range $[-1, 1]$ and arranged as $\mathcal{X} \in \mathbb{R}^d$. We encode input coordinates using Random Fourier Features (RFF) (Rahimi & Recht, 2007; Tancik et al., 2020; He et al., 2024; Rudi & Rosasco, 2017) with $F = 10$ frequencies and scale $\sigma = 1$:

$$\gamma(\mathcal{X}) = [\cos(2\pi\mathbf{B}^\top \mathcal{X}), \sin(2\pi\mathbf{B}^\top \mathcal{X})] \in \mathbb{R}^{2F}, \quad (10)$$

where \mathbf{B} is sampled following the standard Gaussian RFF construction.

5.1. ELM-INR: Qualitative Reconstruction Results

In this section, we compare ELM-INR with representative INR baselines under different training settings.

Qualitative Reconstruction on Standard Image. Figure 4 shows qualitative reconstruction results on the kodim05 image under a standard training protocol. All models are trained for 1000 epochs to reconstruct a 512×512 grayscale image and are evaluated at convergence. While backpropagation-based INR baselines exhibit residual blurring and fail to recover fine-scale structures, ELM-INR achieves near-perfect reconstruction, faithfully capturing both low-frequency content and high-frequency details, as reflected by its substantially higher PSNR.

Multispectral Image Reconstruction. To further evaluate the robustness of INR models beyond standard single- or three-channel standard images, we extend our experiments to high-resolution multispectral satellite imagery. Figure 5 presents a qualitative comparison on a challenging high-frequency crop from a WorldView-3 scene over a Paris Charles de Gaulle Airport (CDG), France, consisting of 8 spectral bands at a spatial resolution of 2048×2048 . All models are trained to regress the full spectral vector at each

spatial coordinate, while only the RGB composite is visualized for clarity. For ELM-INR, we use $S_i = 64^2$ samples per subdomain and an ELM with $m = 4096$ hidden units.

This setting is substantially more demanding than conventional image reconstruction, as the model must simultaneously capture fine-grained spatial details and complex cross-band correlations. As shown in Figure 5, backpropagation-based INR baselines (SIREN, FFN, GaussNet, and WIRE) suffer from pronounced blurring, texture loss, and distortion in high-frequency regions such as edges and man-made structures. These artifacts are indicative of both spectral bias and optimization difficulties when scaling INR training to high-resolution, multi-channel signals.

In contrast, ELM-INR achieves near-perfect reconstruction, faithfully preserving sharp edges and fine structural details across the scene. The substantial PSNR gap highlights the effectiveness of the proposed closed-form, backpropagation-free formulation in handling spectrally complex, multi-band data. These results demonstrate that the advantages of ELM-INR are not limited to standard RGB imagery, but extend naturally to realistic multispectral remote sensing scenarios where iterative INR training becomes increasingly brittle and expensive.

Spatiotemporal PDE Reconstruction. We further evaluate the expressiveness of INR models on a three-dimensional spatiotemporal signal derived from the Navier–Stokes equations. Figure 6 compares volume reconstruction results, where the two horizontal axes correspond to spatial dimensions and the vertical axis represents time. This task is particularly challenging due to the presence of multi-scale structures and rapidly varying dynamics across both space

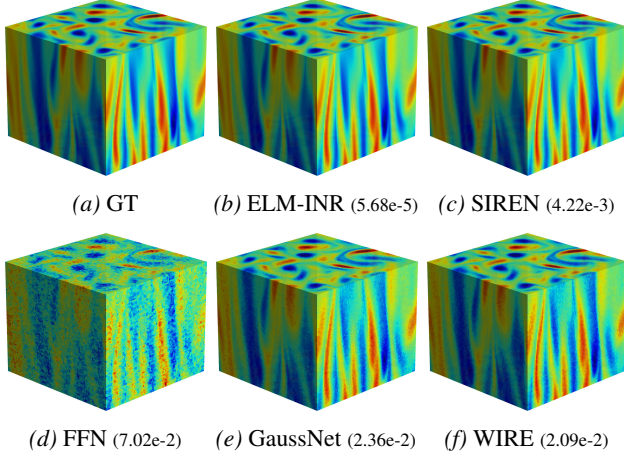


Figure 6. Navier-Stokes equation volume reconstruction results. The horizontal axes are spatial, and the height corresponds to time. Numbers in parentheses denote MAE.

and time.

For this experiment, ELM-INR is configured differently from the image-based settings to explicitly account for temporal structure. Since the temporal dimension contains 100 time steps, the domain is partitioned not only spatially but also along the time axis, with temporal patches of size 10. Each resulting spatiotemporal subdomain is modeled using $S_i = 64^2$ samples and an ELM with $m = 4096$ hidden units, allowing the local models to capture fine-grained temporal variations while maintaining numerical stability.

As shown in Figure 6, backpropagation-based INR baselines fail to accurately recover fine-scale temporal structures. In contrast, ELM-INR achieves a near-exact reconstruction of the full volume, yielding orders-of-magnitude lower error. These results indicate that the proposed closed-form, partitioned representation naturally extends to complex spatiotemporal fields governed by physical dynamics.

Training Efficiency. We analyze reconstruction quality as a function of wall-clock time to compare optimization efficiency across methods. Figure 1 reports PSNR versus runtime on the same image. Backpropagation-based INR baselines improve gradually due to iterative optimization and eventually converge to moderate reconstruction quality. In contrast, ELM-INR reaches very high PSNR within a short runtime, as the solution is obtained via closed-form linear solves rather than iterative gradient updates.

Across different configurations of ELM-INR, we observe consistently fast convergence and high reconstruction quality. Both settings achieve high PSNR within a short runtime, indicating that ELM-INR remains efficient even when varying the number of subdomains and model capacity. These results further emphasize that the proposed method is not

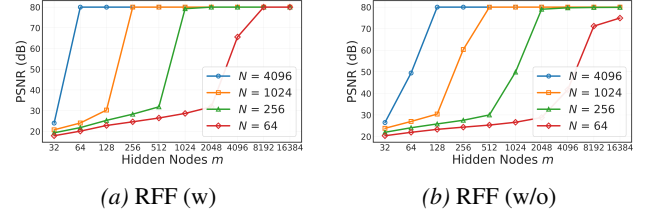


Figure 7. PSNR versus the number of hidden nodes m for different numbers of subdomains N .

only substantially faster than existing INRs, but also robust to reasonable choices of its internal configuration.

5.2. Ablation Study

We conduct an ablation study on the number of basis functions, implemented as the number of hidden nodes m , under different numbers of subdomains N , for ELM-INR using the cameraman image at a resolution of $512 \times 512 \times 1$. Figure 7 reports the reconstruction performance in terms of PSNR as m increases for each choice of N and input representation.

Across all settings, increasing m consistently improves reconstruction quality, but the rate at which performance saturates depends strongly on both the input encoding and the degree of domain decomposition. When Fourier feature mapping is employed (Figure 7a), PSNR saturates rapidly as m increases, indicating that relatively few basis functions are sufficient to capture high-frequency content. In contrast, when raw coordinates are used without Fourier features (Figure 7b), PSNR improves more gradually and requires substantially larger hidden widths to reach saturation.

The effect of domain decomposition is particularly evident when the number of subdomains is small, where each local model must approximate a more complex signal. In this regime, the absence of Fourier features leads to a shift of the saturation point toward larger values of m , reflecting the increased representational burden. Overall, these observations indicate that Fourier feature mapping significantly reduces the required model capacity, while domain decomposition further simplifies local approximation tasks.

Notably, across all configurations, saturation is typically reached when the number of hidden nodes is on the order of the squared subdomain size, i.e., $m \approx |\Omega_i|$. This empirical regularity provides a simple and practical guideline for choosing model capacity, substantially reducing the need for extensive hyperparameter tuning and making ELM-INR easy to configure in practice.

5.3. Effect of BEAM on ELM-INR

Standard Image Reconstruction. Figure 8 demonstrates the effect of BEAM on ELM-INR using the kodim20 im-

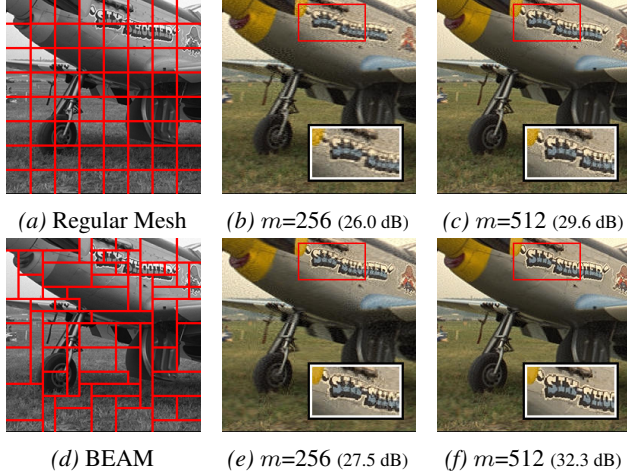


Figure 8. Comparison between ELM-INR without BEAM (top row) and ELM-INR with BEAM (bottom row) on the kodim20 image (256×256).

age. Compared to uniform partitioning, BEAM adaptively refines subdomains by allocating smaller patches to spectrally complex regions and larger patches to smoother areas, resulting in a more balanced partition, as shown in Figure 8 (a and d). For BEAM, the adaptive partition is constructed with an atomic patch size of $s = 32$, while both Regular Mesh and BEAM use the same total number of subdomains, fixed to $N = 64$, ensuring a fair comparison.

This adaptive partitioning leads to consistent reconstruction improvements. For $m = 256$, BEAM improves PSNR from 26.0 dB to 27.5 dB, and for $m = 512$, from 29.6 dB to 32.3 dB, as illustrated in Figure 8 (b, c, e, and f). Visual comparisons further show sharper edges and reduced artifacts with BEAM, particularly in regions with complex structures. These results align with the error bound in Eq. (8), which links reconstruction accuracy to both model capacity and local spectral complexity. While increasing the number of hidden nodes generally improves performance (Figure 7), BEAM provides clear gains at fixed and moderate model capacities by more effectively utilizing available capacity.

Geophysical Field Reconstruction (ERA5). In addition to standard image benchmarks, we further evaluate the effect of BEAM on ELM-INR using full-resolution ERA5 climate data (Hersbach et al., 2020; Rasp et al., 2023). Figure 9 presents reconstruction results on global temperature fields, where each seasonal snapshot has a spatial resolution of latitude = 721 and longitude = 1440. The reconstruction error is measured using mean absolute error (MAE), which is suitable for continuous-valued geophysical fields.

For ERA5 experiments, ELM-INR uses square spatial patches with $S_i = 64^2$ samples per subdomain. When constructing adaptive partitions with BEAM, the atomic

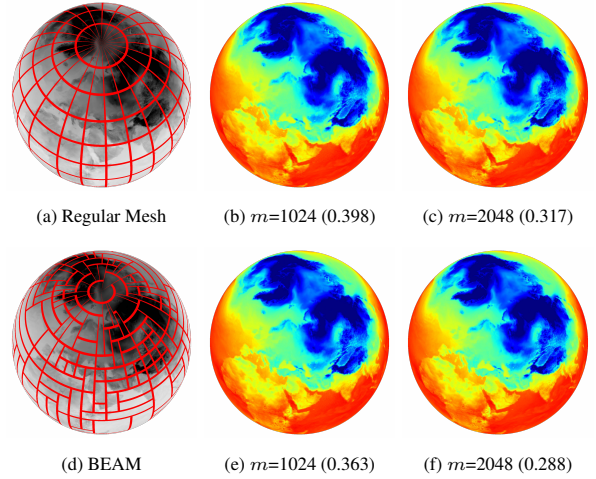


Figure 9. Comparison between ELM-INR without BEAM (top row) and ELM-INR with BEAM (bottom row) on full-resolution ERA5 data (See Appendix G).

patch size is set to $s = 32$. Importantly, to ensure a fair comparison, the total number of subdomains is fixed to be identical for both Regular Mesh and BEAM, with $N = 276$ in all cases. This setting isolates the effect of adaptive partitioning from that of increased model capacity or additional subdomains.

As shown in Figure 9, BEAM consistently reduces reconstruction error compared to uniform partitioning at the same model capacity. For example, in the winter season, BEAM improves MAE from 0.398 to 0.363 for $m = 1024$, and from 0.317 to 0.288 for $m = 2048$. Despite using the same number of subdomains, BEAM allocates smaller patches to spectrally complex regions and larger patches to smoother areas, leading to a more effective use of the fixed representational budget. This further corroborates the role of spectral balancing in improving reconstruction quality under capacity-constrained regimes.

6. Conclusion

In this work, we proposed ELM-INR, a backpropagation-free framework that accelerates INR training by utilizing Extreme Learning Machines with closed-form solutions. We provided a theoretical analysis through the lens of Barron space, demonstrating that approximation error is fundamentally bounded by the local spectral complexity of the target signal. Guided by this insight, we introduced BEAM (Barron-Enhanced Adaptive Mesh refinement), an algorithm that adaptively partitions the domain to equalize spectral energy across subproblems. BEAM proves particularly effective in capacity-constrained regimes, ensuring high-fidelity reconstruction even when the number of hidden neurons (m) is small, by transforming a hard global fit into a set of spectrally balanced, manageable local fits.

References

Adams, R. A. and Fournier, J. J. *Sobolev spaces*, volume 140. Elsevier, 2003.

Anderson, S., Dolean, V., Moseley, B., and Pestana, J. Elmfbpinn: efficient finite-basis physics-informed neural networks. *arXiv preprint arXiv:2409.01949*, 2024.

Babuška, I. and Melenk, J. M. The partition of unity method. *International journal for numerical methods in engineering*, 40(4):727–758, 1997.

Barron, A. R. Universal approximation bounds for superpositions of a sigmoidal function. *IEEE Transactions on Information theory*, 39(3):930–945, 2002.

Barron, J. T., Mildenhall, B., Tancik, M., Hedman, P., Martin-Brualla, R., and Srinivasan, P. P. Mip-nerf: A multiscale representation for anti-aliasing neural radiance fields. In *Proceedings of the IEEE/CVF international conference on computer vision*, pp. 5855–5864, 2021.

Bauer, M., Dupont, E., Brock, A., Rosenbaum, D., Schwarz, J. R., and Kim, H. Spatial functa: Scaling functa to imagenet classification and generation. *arXiv preprint arXiv:2302.03130*, 2023.

Chen, Z., Lu, J., and Lu, Y. On the representation of solutions to elliptic PDEs in Barron spaces. In *Advances in Neural Information Processing Systems*, volume 34, pp. 6454–6465, 2021.

Cho, J., Nam, S., Yang, H., Yun, S.-B., Hong, Y., and Park, E. Separable physics-informed neural networks. *Advances in Neural Information Processing Systems*, 36: 23761–23788, 2023.

Cho, W., Immanuel, S. A., Heo, J., and Kwon, D. Fourier-modulated implicit neural representation for multispectral satellite image compression. *arXiv preprint arXiv:2506.01234*, 2025a.

Cho, W., Jo, M., Lee, K., and Park, N. Neural functions for learning periodic signal. *arXiv preprint arXiv:2506.09526*, 2025b.

De Luigi, L., Cardace, A., Spezialetti, R., Ramirez, P. Z., Salti, S., and Di Stefano, L. Deep learning on implicit neural representations of shapes. *arXiv preprint arXiv:2302.05438*, 2023.

Drusch, M., Del Bello, U., Carlier, S., Colin, O., Fernandez, V., Gascon, F., Hoersch, B., Isola, C., Laberinti, P., Martimort, P., et al. Sentinel-2: Esa’s optical high-resolution mission for gmes operational services. *Remote sensing of Environment*, 120:25–36, 2012.

Dupont, E., Goliński, A., Alizadeh, M., Teh, Y. W., and Doucet, A. Coin: Compression with implicit neural representations. *arXiv preprint arXiv:2103.03123*, 2021.

Dupont, E., Kim, H., Eslami, S., Rezende, D., and Rosenbaum, D. From data to functa: Your data point is a function and you can treat it like one. *arXiv preprint arXiv:2201.12204*, 2022.

Essakine, A., Cheng, Y., Cheng, C.-W., Zhang, L., Deng, Z., Zhu, L., Schönlieb, C.-B., and Aviles-Rivero, A. I. Where do we stand with implicit neural representations? a technical and performance survey. *arXiv preprint arXiv:2411.03688*, 2024.

He, M., He, F., Liu, F., and Huang, X. Random fourier features for asymmetric kernels. *Machine Learning*, 113(11):8459–8485, 2024.

Hersbach, H., Bell, B., Berrisford, P., Hirahara, S., Horányi, A., Muñoz-Sabater, J., Nicolas, J., Peubey, C., Radu, R., Schepers, D., et al. The era5 global reanalysis. *Quarterly journal of the royal meteorological society*, 146(730): 1999–2049, 2020.

Hildebrand, F. B. *Introduction to numerical analysis*. Courier Corporation, 1987.

Huang, G.-B., Zhu, Q.-Y., and Siew, C.-K. Extreme learning machine: theory and applications. *Neurocomputing*, 70(1-3):489–501, 2006.

Huang, G.-B., Wang, D. H., and Lan, Y. Extreme learning machines: a survey. *International journal of machine learning and cybernetics*, 2(2):107–122, 2011.

Jo, M., Cho, W., Mudiyanselage, U. B., Lee, S., Park, N., and Lee, K. Pdefuncta: Spectrally-aware neural representation for pde solution modeling. *arXiv preprint arXiv:2506.12790*, 2025.

Karniadakis, G. E., Kevrekidis, I. G., Lu, L., Perdikaris, P., Wang, S., and Yang, L. Physics-informed machine learning. *Nature Reviews Physics*, 3(6):422–440, 2021.

Kingma, D. P. Adam: A method for stochastic optimization. *arXiv preprint arXiv:1412.6980*, 2014.

Krishnapriyan, A., Gholami, A., Zhe, S., Kirby, R., and Mahoney, M. W. Characterizing possible failure modes in physics-informed neural networks. *Advances in neural information processing systems*, 34:26548–26560, 2021.

Lee, K., Trask, N. A., Patel, R. G., Gulian, M. A., and Cyr, E. C. Partition of unity networks: deep hp-approximation. *arXiv preprint arXiv:2101.11256*, 2021.

Liao, Y. and Ming, P. Spectral baron space for deep neural network approximation. *SIAM Journal on Mathematics of Data Science*, 7(3):1053–1076, 2025.

Ma, C., Wu, L., et al. The baron space and the flow-induced function spaces for neural network models. *Constructive Approximation*, 55(1):369–406, 2022.

Ma, Q., Paudel, D. P., Konukoglu, E., and Van Gool, L. Implicit-zoo: A large-scale dataset of neural implicit functions for 2d images and 3d scenes. *arXiv preprint arXiv:2406.17438*, 2024.

Marwah, T., Lipton, Z. C., Lu, J., and Risteski, A. Neural network approximations of pdes beyond linearity: A representational perspective. In *International Conference on Machine Learning*, pp. 24139–24172. PMLR, 2023.

Maz’ya, V. *Sobolev spaces*. Springer, 2013.

Melenk, J. M. and Babuška, I. The partition of unity finite element method: basic theory and applications. *Computer methods in applied mechanics and engineering*, 139(1-4):289–314, 1996.

Mildenhall, B., Srinivasan, P. P., Tancik, M., Barron, J. T., Ramamoorthi, R., and Ng, R. Nerf: Representing scenes as neural radiance fields for view synthesis. *Communications of the ACM*, 65(1):99–106, 2021.

Molaei, A., Aminimehr, A., Tavakoli, A., Kazerouni, A., Azad, B., Azad, R., and Merhof, D. Implicit neural representation in medical imaging: A comparative survey. In *Proceedings of the IEEE/CVF International Conference on Computer Vision*, pp. 2381–2391, 2023.

Moseley, B., Markham, A., and Nissen-Meyer, T. Finite basis physics-informed neural networks (fbpinns): a scalable domain decomposition approach for solving differential equations. *arXiv preprint arXiv:2107.07871*, 2021.

Paszke, A., Gross, S., Massa, F., Lerer, A., Bradbury, J., Chanan, G., Killeen, T., Lin, Z., Gimelshein, N., Antiga, L., et al. Pytorch: An imperative style, high-performance deep learning library. *Advances in neural information processing systems*, 32, 2019.

Pumarola, A., Corona, E., Pons-Moll, G., and Moreno-Noguer, F. D-nerf: Neural radiance fields for dynamic scenes. In *Proceedings of the IEEE/CVF conference on computer vision and pattern recognition*, pp. 10318–10327, 2021.

Rahaman, N., Baratin, A., Arpit, D., Draxler, F., Lin, M., Hamprecht, F., Bengio, Y., and Courville, A. On the spectral bias of neural networks. In *International conference on machine learning*, pp. 5301–5310. PMLR, 2019.

Rahimi, A. and Recht, B. Random features for large-scale kernel machines. *Advances in neural information processing systems*, 20, 2007.

Raissi, M., Perdikaris, P., and Karniadakis, G. E. Physics-informed neural networks: A deep learning framework for solving forward and inverse problems involving nonlinear partial differential equations. *Journal of Computational physics*, 378:686–707, 2019.

Ramasinghe, S. and Lucey, S. Beyond periodicity: Towards a unifying framework for activations in coordinate-mlps. In *European Conference on Computer Vision*, pp. 142–158. Springer, 2022.

Rasp, S., Hoyer, S., Merose, A., Langmore, I., Battaglia, P., Russel, T., Sanchez-Gonzalez, A., Yang, V., Carver, R., Agrawal, S., Chantry, M., Bouallegue, Z. B., Dueben, P., Bromberg, C., Sisk, J., Barrington, L., Bell, A., and Sha, F. Weatherbench 2: A benchmark for the next generation of data-driven global weather models, 2023.

Reddy, J. N. An introduction to the finite element method. *New York*, 27(14), 1993.

Rudi, A. and Rosasco, L. Generalization properties of learning with random features. *Advances in neural information processing systems*, 30, 2017.

Saragadam, V., LeJeune, D., Tan, J., Balakrishnan, G., Veeraraghavan, A., and Baraniuk, R. G. Wire: Wavelet implicit neural representations. In *Proceedings of the IEEE/CVF Conference on Computer Vision and Pattern Recognition*, pp. 18507–18516, 2023.

Sitzmann, V., Martel, J., Bergman, A., Lindell, D., and Wetzstein, G. Implicit neural representations with periodic activation functions. *Advances in neural information processing systems*, 33:7462–7473, 2020.

Tancik, M., Srinivasan, P., Mildenhall, B., Fridovich-Keil, S., Raghavan, N., Singhal, U., Ramamoorthi, R., Barron, J., and Ng, R. Fourier features let networks learn high frequency functions in low dimensional domains. *Advances in neural information processing systems*, 33:7537–7547, 2020.

Yüce, G., Ortiz-Jiménez, G., Besbinar, B., and Frossard, P. A structured dictionary perspective on implicit neural representations. In *Proceedings of the IEEE/CVF Conference on Computer Vision and Pattern Recognition*, pp. 19228–19238, 2022.

Zheng, H., Chu, W., Zhang, B., Wu, Z., Wang, A., Feng, B. T., Zou, C., Sun, Y., Kovachki, N., Ross, Z. E., et al. Inversebench: Benchmarking plug-and-play diffusion priors for inverse problems in physical sciences. *arXiv preprint arXiv:2503.11043*, 2025.

A. Symbol Definitions

Table 1 provides a consolidated summary of the mathematical symbols used throughout the paper.

Table 1. Summary of symbols used throughout the paper.

Symbol	Description
Global function and domain notation	
$\mathcal{X} \in \mathbb{R}^d$	Continuous input coordinate in d -dimensional space
$f(\mathcal{X})$	Ground-truth target function
$\hat{f}(\mathcal{X})$	Global ELM-INR approximation of f
d	Input dimensionality
$\Omega \subset \mathbb{R}^d$	Global spatial domain
Domain decomposition and partition-of-unity (PoU)	
Ω_i	i -th local subdomain of Ω
N	Number of subdomains in the partition
$\phi_i(\mathcal{X})$	Partition-of-unity window function associated with Ω_i
$\text{supp}(\phi_i)$	Support of the PoU function ϕ_i
Local Extreme Learning Machine (ELM) representation	
$\hat{f}_i(\mathcal{X})$	Local ELM approximation on subdomain Ω_i
m	Number of hidden neurons (ELM width)
$\sigma(\cdot)$	Activation function
$w_{i,j}$	Fixed random input weight of neuron j in Ω_i
$b_{i,j}$	Fixed random bias of neuron j in Ω_i
$\alpha_{i,j}$	Trainable output weight of neuron j in Ω_i
α_i	Output weight vector for the i -th local ELM
ELM training and least-squares formulation	
S_i	Number of training samples in subdomain Ω_i
$\mathbf{H}_i \in \mathbb{R}^{S_i \times m}$	Hidden-layer activation matrix for Ω_i
$\mathbf{y}_i \in \mathbb{R}^{S_i}$	Target values sampled from f on Ω_i
Barron space and spectral complexity measures	
$\mathcal{F}(\xi)$	Fourier transform of function f
$\xi \in \mathbb{R}^d$	Continuous frequency variable
Γ	Fourier-based Barron function class
\mathcal{B}	Barron space
$\ f\ _{\mathcal{B}}$	Barron norm of function f
$\ f\ _{\mathcal{B}_S}$	Spectral Barron norm of function f
β_i	Local spectral Barron norm on subdomain Ω_i
Approximation error and theoretical bounds	
C	Constant independent of network width m
$\ \cdot\ _{L^2(\Omega)}$	L^2 norm over domain Ω
BEAM algorithm and adaptive partitioning	
\mathcal{P}	Adaptive partition of the domain produced by BEAM
τ	Spectral Barron norm threshold used in BEAM
s	Atomic cell size for BEAM initialization
E_{new}	Spectral energy after merging two subdomains
k	Discrete frequency index in the DFT domain
$\mathcal{F}_i(k)$	Discrete Fourier coefficient on subdomain Ω_i

B. Limitations and Future Works

Despite its advantages, ELM-INR shares a fundamental limitation with implicit neural representations in general: the model is trained on a per-instance basis. That is, each target function requires a separate fitting process, and the learned parameters do not directly generalize across different target instances. While this instance-specific formulation is a key strength of INRs for high-fidelity signal representation, it also limits their applicability in settings that demand rapid adaptation across large collections of signals.

Since ELM-INR operates on general coordinate-based representations, it naturally extends to higher-dimensional neural fields such as neural radiance fields (NeRFs), spatiotemporal fields, and other continuous implicit representations. In particular, integrating BEAM-style adaptive partitioning with neural field models could help address spectral imbalance and capacity limitations in large-scale 3D or 4D scenes. Investigating such extensions, including applications to view synthesis and dynamic scene modeling, constitutes an important direction for future work.

C. Detailed Experimental Setups

Software and hardware environments. All experiments were conducted on a workstation equipped with a single NVIDIA A6000 GPU (48 GB VRAM), an AMD EPYC 9224 24-core CPU (96 logical cores), and 377 GB of system memory. The software environment is based on Ubuntu 20.04.6 LTS with Python 3.12.7. We use PyTorch 2.7.0 compiled with CUDA 12.6 for all experiments.

Hyperparameter settings. All baseline INRs are optimized using the Adam optimizer with default momentum parameters and no weight decay. All models are trained for a fixed number of optimization steps depending on the task: 1000 steps for standard image datasets, 3000 steps for Navier–Stokes experiments, and 10,000 steps for remote-sensing datasets.

Rather than fixing a single hyperparameter configuration per model, we perform a lightweight hyperparameter search over a common set of architectural and optimization parameters. Specifically, the number of hidden nodes is selected from $\{256, 512, 1024\}$, the number of hidden layers from $\{3, 4, 5\}$, and the learning rate from $\{5 \times 10^{-5}, 1 \times 10^{-4}\}$. For each baseline, we report results using the best-performing configuration.

All remaining model-specific hyperparameters—such as activation functions, frequency or bandwidth parameters, and feature encodings—are set according to the original configurations recommended in the respective papers.

ELM-INR. ELM-INR uses fixed hyperparameters within each data modality. For standard image experiments, we set the subdomain size to $S_i = 32^2$ and the number of hidden nodes to $m = 1024$. For multispectral remote-sensing images and Navier–Stokes experiments, we use a larger configuration with $S_i = 64^2$ and $m = 4096$.

PSNR computation. Reconstruction quality is evaluated using the peak signal-to-noise ratio (PSNR). Following our implementation, predictions and ground-truth signals are first normalized by the maximum value of the ground truth. The PSNR is then computed as

$$\text{PSNR} = -10 \log_{10}(\text{MSE} + \varepsilon),$$

where MSE denotes the mean squared error over all evaluated samples and ε is a small constant for numerical stability. In all experiments, we set $\varepsilon = 10^{-8}$. For multispectral images, PSNR is computed independently for each channel and the final score is reported as the average across channels.

D. Dataset Description: Navier–Stokes Equation

We use the same $(2 + 1)$ D incompressible Navier–Stokes dataset as in SPINN (Cho et al., 2023). The dataset consists of a single spatio-temporal scalar field sampled on a uniform grid of size $n_x \times n_y \times n_t = 128 \times 128 \times 100$, where the first two axes correspond to the spatial coordinates (x_1, x_2) and the third axis corresponds to time t .

Governing equation and setting. Let $\mathcal{X} = (x_1, x_2, t) \in [0, 2\pi]^2 \times [0, 1]$ denote the space–time coordinate. Following SPINN (Cho et al., 2023), we consider a decaying-turbulence setting (no external forcing) for the $(2 + 1)$ D incompressible NS dynamics in the vorticity formulation:

$$\partial_t \omega(\mathcal{X}) + u(\mathcal{X}) \cdot \nabla \omega(\mathcal{X}) = \nu \Delta \omega(\mathcal{X}), \quad \nabla \cdot u(\mathcal{X}) = 0, \quad \omega(\mathcal{X}) = \partial_{x_1} u_2(\mathcal{X}) - \partial_{x_2} u_1(\mathcal{X}), \quad (11)$$

where $u(\mathcal{X}) = (u_1(\mathcal{X}), u_2(\mathcal{X}))$ is the 2D velocity field, and we fix the viscosity to $\nu = 0.01$.

Numerical generation and learning pairs. A reference solution is generated using a pseudo-spectral CFD solver (JAX-CFD) with periodic boundary conditions in space. The initial condition is sampled from a Gaussian random field (with maximum velocity 5 in the SPINN setup), and the resulting field is recorded on the uniform grid over $[0, 2\pi]^2 \times [0, 1]$. For training coordinate-based models, each grid point induces a coordinate–value pair $(\mathcal{X}_{ijk}, \mathbf{y}_{ijk})$, where \mathbf{y}_{ijk} denotes the sampled scalar value at \mathcal{X}_{ijk} . We linearly normalize each coordinate axis to $[-1, 1]$ before feeding it to the network.

E. Computational Complexity Analysis

We analyze the computational cost of ELM-INR in contrast to standard backpropagation-based INRs such as SIREN, FFN, and WIRE.

To formalize this comparison, let S denote the total number of coordinate samples (e.g., pixels) in the domain, and let $\{\Omega_i\}_{i=1}^N$ be a partition of the domain, where each subdomain Ω_i contains S_i samples such that $\sum_{i=1}^N S_i = S$. We assume each local ELM utilizes m hidden units and outputs C channels. For the comparative analysis of backpropagation-based INRs, we denote the number of hidden layers by L and the total number of training iterations by T .

ELM-INR (Closed-Form): For each subdomain Ω_i , ELM-INR constructs a hidden activation matrix $\mathbf{H}_i \in \mathbb{R}^{S_i \times m}$ and solves a linear least-squares problem for the output weights. The dominant computational cost arises from forming the normal matrix $\mathbf{H}_i^\top \mathbf{H}_i$ and solving the resulting linear system. The cost per subdomain is therefore $\mathcal{O}(S_i m^2 + m^3)$, where the $S_i m^2$ term dominates in the typical regime where $S_i \gg m$. Summing over all subdomains yields the total cost:

$$\mathcal{O}\left(\sum_{i=1}^N (S_i m^2 + m^3)\right) = \mathcal{O}(Sm^2 + Nm^3). \quad (12)$$

In standard INR settings, where $S \gg m$ and the number of partitions $N \ll S$, the overall cost is effectively linear in the number of samples S , up to a quadratic dependence on the hidden width m . Importantly, this cost is incurred only once, as ELM-INR does not rely on iterative optimization.

Backpropagation-Based INR: For a standard INR trained via backpropagation, each training iteration consists of a forward pass, a backward pass, and a parameter update. For a network with L hidden layers of width m , the computational cost per iteration scales as $\mathcal{O}(LSm^2)$, where the quadratic dependence on m arises from the dense matrix multiplications between hidden layers. Over T training iterations, the total computational cost becomes $\mathcal{O}(TLSm^2)$.

Comparison: Comparing the two costs, ELM-INR replaces the iterative multiplicative factor $T \times L$ with a linear-algebraic solve. In practice, since the number of iterations T is typically on the order of thousands and the depth $L \geq 2$ for expressive INRs, this difference results in orders-of-magnitude computational savings.

F. Additional Experimental Results

Interpretation of training dynamics. Figure 10 illustrates the evolution of PSNR across training steps for SIREN, FFN, GaussNet, WIRE, and ELM-INR on kodim08, kodim20, kodim24, and cameraman. Solid lines denote mean performance and shaded regions indicate variability. ELM-INR achieves stable high-quality reconstruction without iterative backpropagation. Unlike backpropagation-based INRs, ELM-INR does not rely on iterative optimization. Its parameters are obtained via a single closed-form least-squares solve, and therefore it does not admit intermediate training states. For visualization purposes, the ELM-INR curve is replicated across the step axis to highlight the absence of training dynamics.

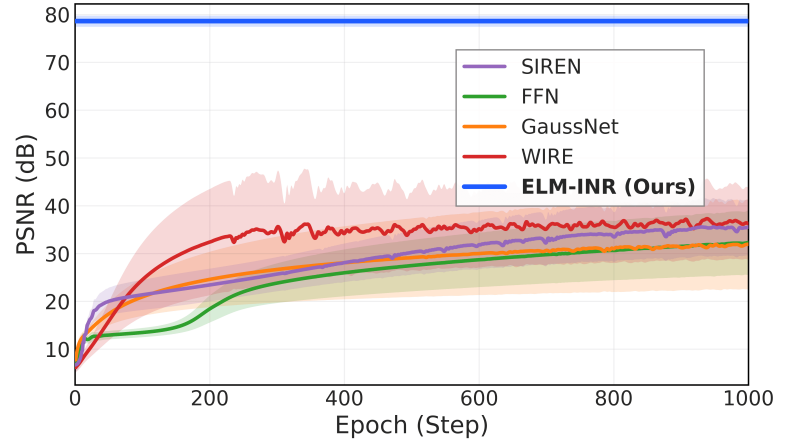


Figure 10. Training dynamics of different INR architectures.

F.1. General Dataset in Computer Vision



Figure 11. Additional qualitative comparison on the kodim08 image. (512 × 512)

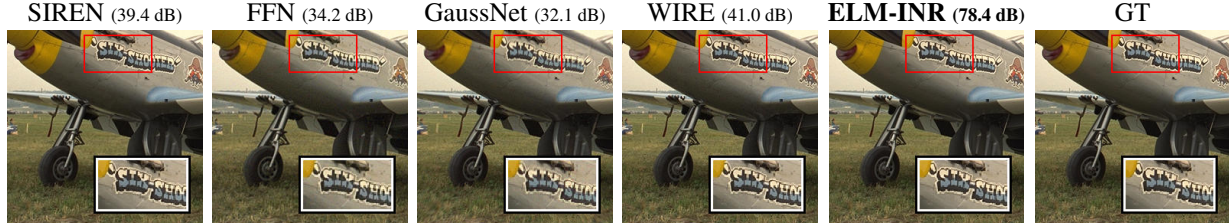


Figure 12. Additional qualitative comparison on the kodim20 image. (256 × 256)

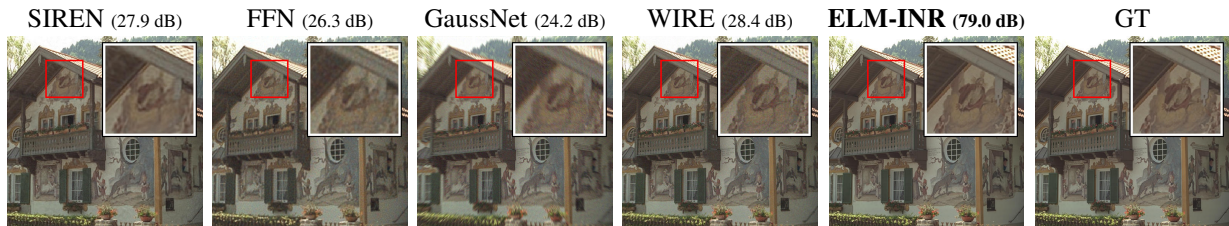


Figure 13. Additional qualitative comparison on the kodim24 image. (512 × 512)

We provide additional qualitative and efficiency comparisons on representative standard images from the Kodak dataset, including kodim08, kodim20, and kodim24. As shown in Figures 11–13, ELM-INR consistently achieves high-fidelity reconstructions across all datasets, accurately recovering fine-scale structures that are blurred or distorted by backpropagation-based INR baselines.

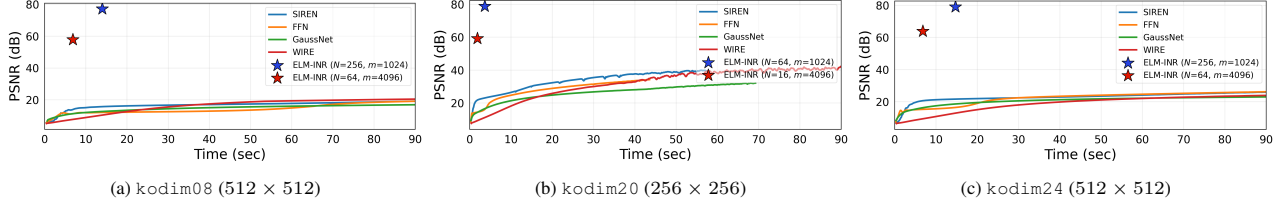


Figure 14. PSNR as a function of wall-clock time for different INR models on representative images. ELM-INR achieves substantially higher reconstruction quality within a short inference time compared to iterative INRs.

Figure 14 further reports PSNR as a function of wall-clock time. While iterative INR methods exhibit gradual improvement due to repeated optimization steps, ELM-INR attains substantially higher PSNR within a short runtime, reflecting its closed-form, backpropagation-free training. These results demonstrate that the proposed method is both highly effective and computationally efficient across a range of standard computer vision benchmarks.

F.2. Qualitative Comparison under a CO₂ Emission Budget

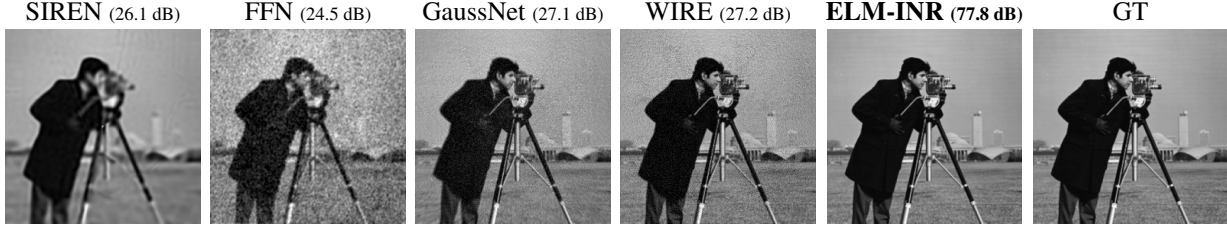


Figure 15. Qualitative comparison on the cameraman grayscale image (256 x 256) under CO₂-constrained training. ELM-INR is used as the reference, while baseline INR methods (SIREN, FFN, GaussNet, and WIRE) are trained with up to 10× larger CO₂ emission budgets. PSNR values are reported next to each method, illustrating the reconstruction quality achieved under fixed environmental constraints.

Table 2. CO₂-constrained training results on the cameraman. Metrics are reported under increasing CO₂ budgets relative to ELM-INR.

Metric	CO ₂ ×	FFN	GaussNet	SIREN	WIRE	ELM-INR
PSNR (dB)	1 ×	11.5	11.7	20.2	5.8	77.8
	5 ×	13.1	16.0	25.1	9.1	–
	10 ×	14.9	19.4	27.1	13.4	–
Steps	1 ×	20	11	34	5	–
	5 ×	92	48	79	28	–
	10 ×	178	93	135	54	–
Time (s)	1 ×	0.36	0.38	1.01	0.37	3.75
	5 ×	1.55	1.63	2.18	1.70	–
	10 ×	2.99	3.15	3.62	3.20	–
CO ₂ (kg)	1 ×	1.18×10^{-5}	1.15×10^{-5}	1.21×10^{-5}	1.14×10^{-5}	1.13×10^{-5}
	5 ×	5.69×10^{-5}	5.80×10^{-5}	5.70×10^{-5}	5.87×10^{-5}	–
	10 ×	1.13×10^{-4}	1.15×10^{-4}	1.13×10^{-4}	1.15×10^{-4}	–

This subsection evaluates the computational efficiency of ELM-INR under explicit CO₂ emission constraints. All experiments are conducted on a single NVIDIA A6000 GPU, and CO₂ emissions are estimated from measured wall-clock time using a consistent hardware-dependent conversion. Figure 15 presents a qualitative comparison on the cameraman image under matched and increased CO₂ budgets, while Table 2 reports the corresponding reconstruction quality, runtime, and emission statistics.

As summarized in Table 2, backpropagation-based INR methods exhibit gradual improvements as the CO₂ budget increases, but their gains remain limited even at significantly higher emission levels. In contrast, ELM-INR achieves substantially higher reconstruction quality with a single closed-form solve, highlighting a fundamentally different efficiency profile under constrained computational and environmental budgets.

F.3. WorldView-3 8-band Visualizations

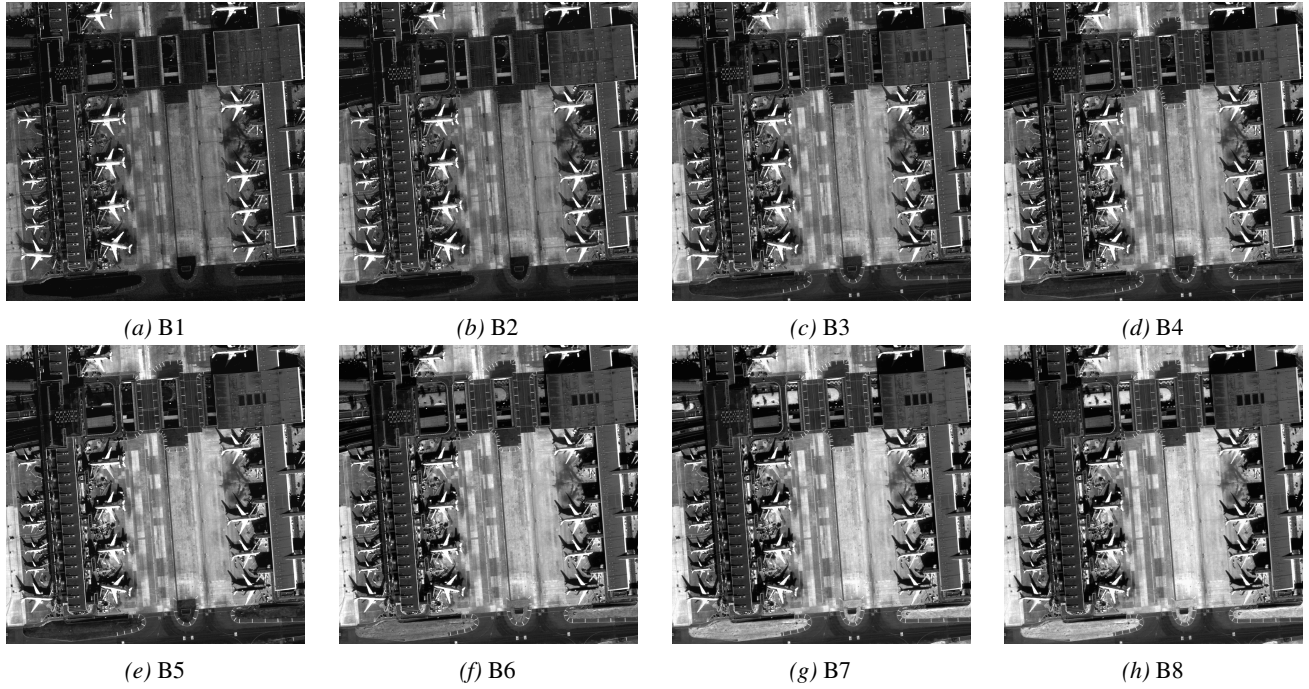


Figure 16. Grayscale visualization of the eight spectral bands (B1–B8) from a WorldView-3 multispectral image capturing the Charles de Gaulle Airport (CDG).

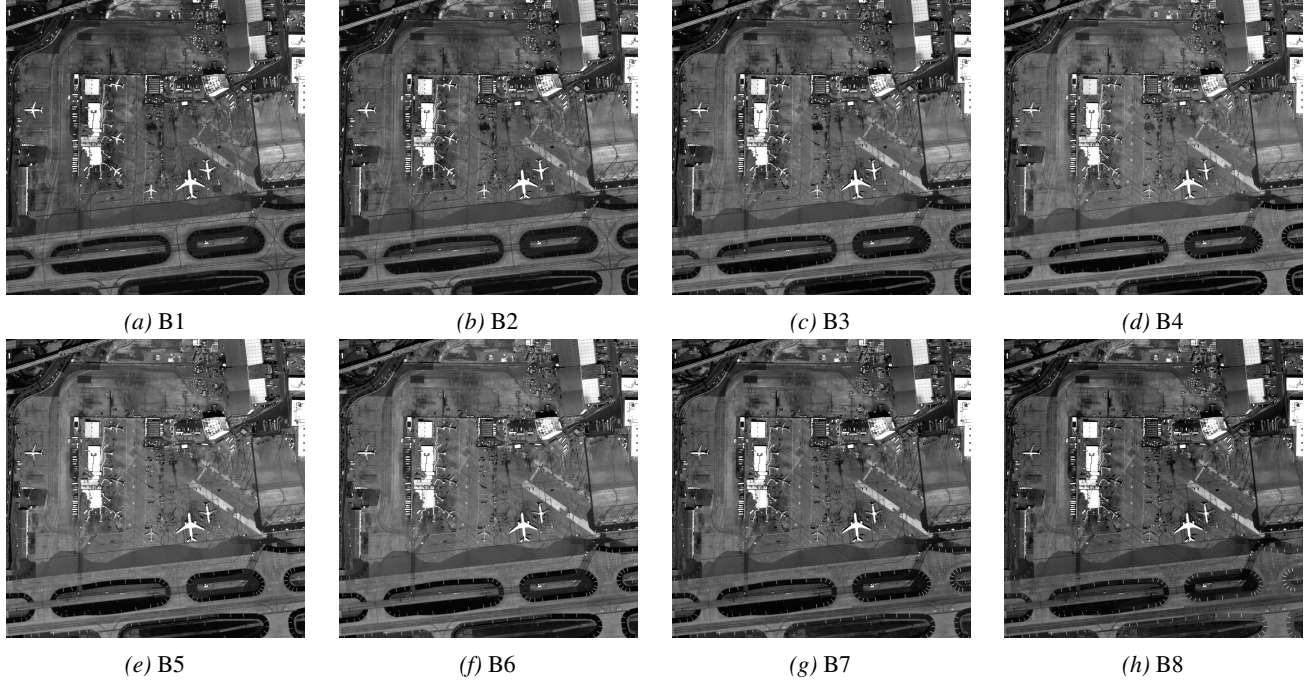


Figure 17. Grayscale visualization of the eight spectral bands (B1–B8) from a WorldView-3 multispectral image capturing the Los Angeles International Airport (LAX).

To improve reproducibility and provide visual context for our multispectral experiments, we include the two WorldView-3 scenes used in this study. For each scene, we visualize all eight multispectral bands individually. These visualizations

highlight band-specific visual patterns and help interpret reconstruction behavior under multi-band supervision. Figures 16 and 17 show the eight-band decompositions for the two scenes.

F.4. Experimental Results on Multispectral Satellite Imagery

Beyond standard computer-vision benchmarks (i.e., 1-channel grayscale or 3-channel RGB images), we additionally evaluate ELM-INR on multispectral satellite imagery with a substantially larger number of channels. The input is a 2D spatial coordinate $\mathcal{X} = (x_1, x_2)$ on the image plane and the output is the per-pixel spectral vector $V(\mathcal{X}) \in \mathbb{R}^C$. For all satellite experiments, we train the INR by regressing the full spectral vector at each coordinate; for qualitative visualization, we only display the RGB composite. Since satellite scenes are typically higher-resolution and contain diverse, fine-grained structures within a single frame, we train all baseline INR models for 10,000 epochs to ensure fair and stable convergence. We additionally perform basic hyperparameter tuning for each baseline (e.g., hidden dimension, number of layers, and learning rate) under this longer training schedule.

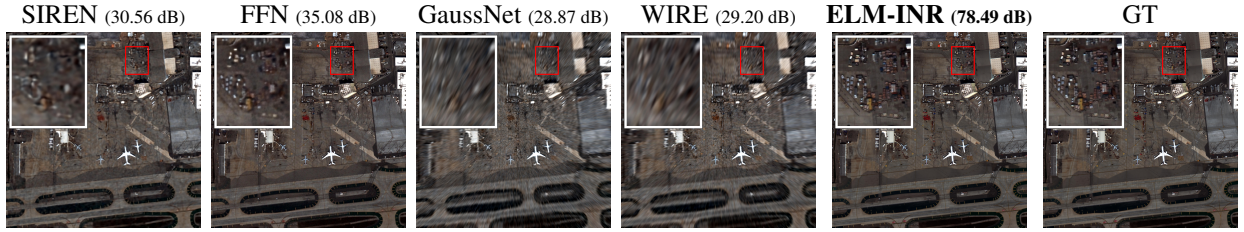


Figure 18. Qualitative comparison on a high-frequency region from a WorldView-3 multispectral image. The image consists of 8 spectral bands with a spatial resolution of 2048×2048 pixels, while the visualization shows only the RGB channels for clarity. ELM-INR achieves substantially higher reconstruction fidelity, recovering fine-grained structures that are heavily blurred or distorted by baseline INR models.

Table 3. WorldView-3 8-Band Specifications and Usage

Band	Description	Wave. Range (nm)	Primary Usage
B1	Coastal	400 – 450	Coastal monitoring and atmospheric correction
B2	Blue	450 – 510	Aerosol/haze effects and water quality cues
B3	Green	510 – 580	Vegetation vigor and true-color rendering
B4	Yellow	585 – 625	Vegetation stress and chlorosis cues
B5	Red	630 – 690	Chlorophyll absorption and vegetation discrimination
B6	Red Edge	705 – 745	Chlorophyll-related sensitivity and crop condition monitoring
B7	NIR-1	770 – 895	Biomass estimation, soil moisture, water body delineation
B8	NIR-2	860 – 1040	Vegetation and moisture-related sensitivity

WorldView-3. Figure 18 illustrates a high-frequency crop from a WorldView-3 multispectral scene (a commercial satellite operated by Maxar Technologies, formerly DigitalGlobe) covering the Los Angeles International Airport (LAX). The sample consists of $C = 8$ spectral bands and is processed at a spatial resolution of 2048×2048 pixels. As shown in Figure 18, the airport area contains complex man-made structures such as runways, taxiways, and buildings, which induce strong high-frequency components. This makes the region a particularly challenging testbed for evaluating spectral bias in implicit neural representations.

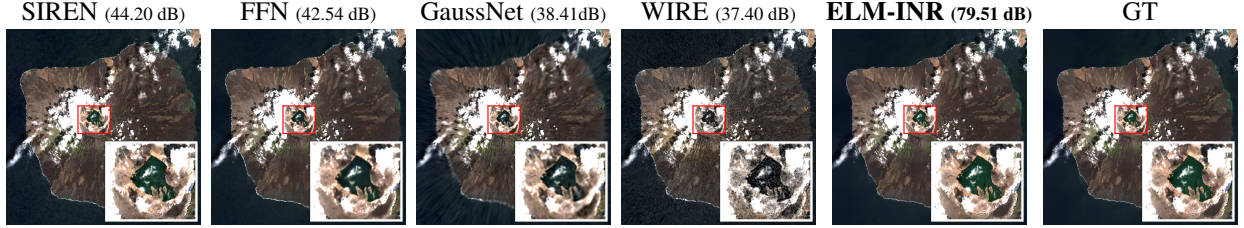


Figure 19. Qualitative comparison on a high-frequency region from a Sentinel-2 L2A multispectral image (Drusch et al., 2012). The image consists of 12 spectral bands with a spatial resolution of 2048×2048 pixels, while the visualization shows only the RGB channels for clarity. ELM-INR achieves substantially higher reconstruction fidelity, recovering fine-grained structures that are heavily blurred or distorted by baseline INR models.

Table 4. Multispectral Bands in Sentinel-2 Satellite Imagery

Band	Description	Wave. Range (nm)	Primary Usage
B1	Coastal aerosol	433–453	Atmospheric correction
B2	Blue	458–523	Water body analysis
B3	Green	543–578	Vegetation monitoring
B4	Red	650–680	Vegetation and soil analysis
B5	Red-edge 1	698–713	Vegetation monitoring
B6	Red-edge 2	733–748	Vegetation structure analysis
B7	Red-edge	773–793	Vegetation chlorophyll assessment
B8	NIR	785–900	Biomass and vegetation vigor monitoring
B8A	Narrow-NIR	855–875	Vegetation monitoring
B9	Water vapour	935–955	Cloud screening and water vapour analysis
B11	SWIR	1565–1655	Cloud and snow monitoring
B12	SWIR	2100–2280	Soil and water content analysis

Sentinel-2. Figure 19 shows a Sentinel-2 Level-2A multispectral image capturing the Galápagos Islands. The sample contains $C = 12$ spectral bands and is processed at a spatial resolution of 2048×2048 pixels. As illustrated in Figure 19, sharp island–ocean boundaries and heterogeneous land-cover patterns introduce localized high-frequency structures, making this scene well-suited for evaluating reconstruction fidelity in a multi-band setting. Following the WorldView-3 experiment, only the RGB channels are visualized for clarity, while the INR is trained to predict the full spectral vector at each spatial coordinate.

E.5. Experimental Results on MRI data

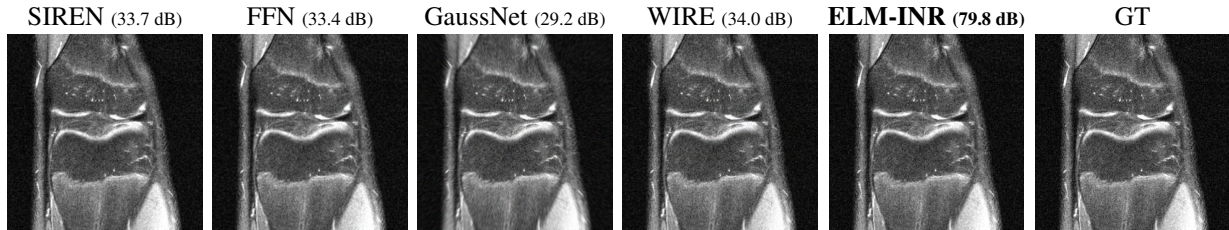


Figure 20. Qualitative comparison on an MRI image with a spatial resolution of 512×512 .

We further evaluate ELM-INR on MRI data using the dataset setup from InverseBench (Zheng et al., 2025). In MRI, the raw measurements are acquired in the frequency domain (k-space) and are intrinsically complex-valued; in modern protocols, data are often collected with multiple receiver coils, yielding multi-coil k-space observations where each coil has a distinct

spatial sensitivity profile. In compressed-sensing MRI, k-space is subsampled, and the resulting inverse problem produces structured aliasing artifacts unless appropriately reconstructed.

G. Additional Experiments: BEAM in Capacity-Limited Regimes

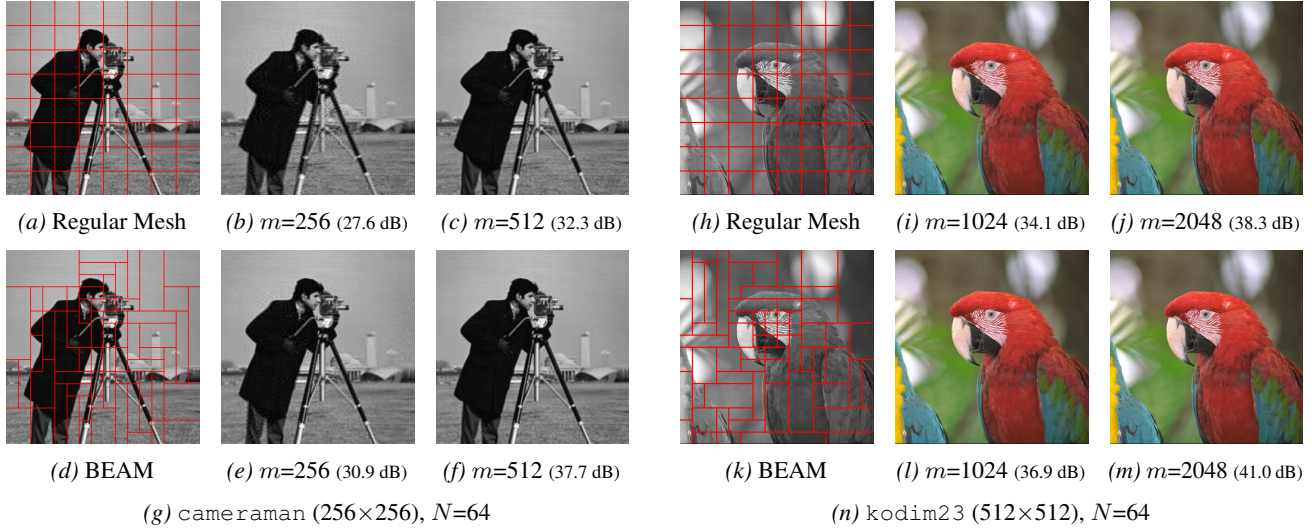


Figure 21. Side-by-side comparison of ELM-INR without BEAM (top rows) and with BEAM (bottom rows) on standard images. BEAM consistently improves reconstruction quality at identical model capacity m .

This section provides additional evidence of the effectiveness of BEAM in capacity-limited settings for ELM-INR. BEAM is designed to be most beneficial when the number of hidden nodes m per local ELM is small, as reconstruction quality in this regime is dominated by the most spectrally complex regions (cf. Eq. (8)). By adaptively refining only difficult regions while allocating larger patches to smoother areas, BEAM enables a more effective use of a fixed budget of basis functions than uniform (regular) partitioning.

Figure 21 follows the same experimental protocol as in the main paper (e.g., Figures 8–9), comparing ELM-INR with a regular mesh (top rows) against ELM-INR coupled with BEAM (bottom rows) at identical model capacity m . For the cameraman image (256×256), we use spatial patches with $S_i = 32^2$ samples, resulting in $N = 64$ subdomains, and construct BEAM with an atomic size of $s = 16$. Experiments are conducted for $m = 256$ and $m = 512$. For the kodim23 image (512×512), we use larger patches with $S_i = 64^2$, again fixing the number of subdomains to $N = 64$, and set the atomic size to $s = 32$, with model capacities $m = 1024$ and $m = 2048$.

Across both datasets, BEAM consistently improves reconstruction quality, with especially pronounced gains at smaller m , where uniform partitioning tends to underfit localized high-frequency content such as edges and textured regions. In contrast, when m is sufficiently large, reconstruction performance saturates, as also observed in the main experiments, leaving less room for improvement through adaptive partitioning. This behavior highlights that BEAM is particularly effective in regimes where model capacity is constrained.

We further evaluate BEAM on full-resolution ERA5 data. For these experiments, ELM-INR uses spatial patches with $S_i = 64^2$ samples and BEAM is constructed with an atomic size of $s = 32$. Figure 23 (Figure 17 in the main figure numbering) reports seasonal reconstructions with and without BEAM for two capacities ($m = 1024$ and $m = 2048$). Across all seasons, BEAM consistently reduces the mean absolute error (MAE) at both capacities, with relatively larger improvements in the more capacity-constrained setting ($m = 1024$). These results further corroborate that BEAM is most impactful when the underlying ELM-INR operates under limited representational budget.

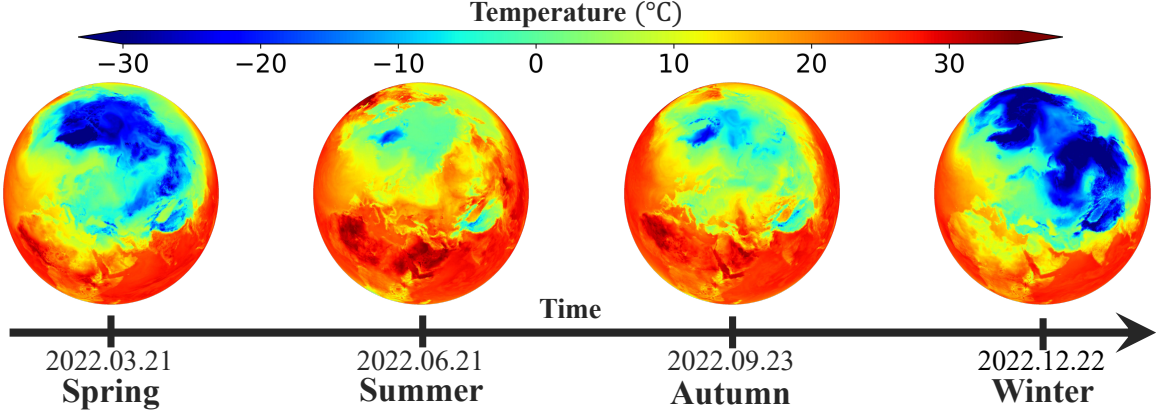


Figure 22. ERA5 dataset samples. Visualization of the ERA5 reanalysis data used in our experiments. We select four snapshots from 2022 corresponding to the vernal equinox, summer solstice, autumnal equinox, and winter solstice. Each panel shows the 2 m air temperature field, highlighting seasonal variability and serving as the target signal for our reconstruction benchmarks.

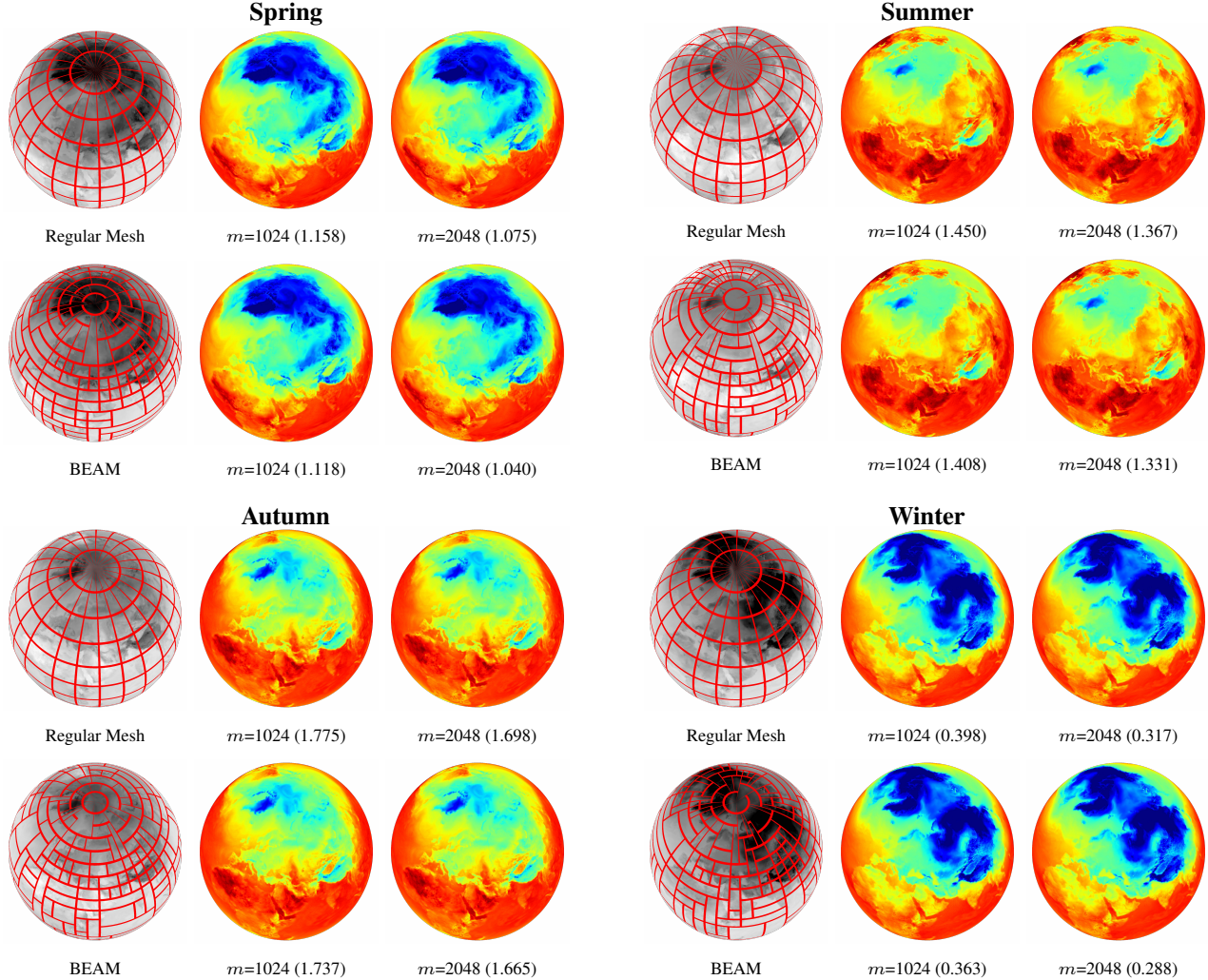


Figure 23. Seasonal comparison of ELM-INR without BEAM (top row in each block) and with BEAM (bottom row in each block) on full-resolution ERA5 data. For identical model capacity ($m = 1024$ or $m = 2048$), BEAM consistently reduces MAE across all seasons by adaptively refining spectrally complex regions.